Tellus
SERIES A
DYNAMIC
METEOROLOGY
AND OCEANOGRAPHY
PUBLISHED BY THE INTERNATIONAL METEOROLOGICAL INSTITUTE IN STOCKHOLM

Tellus (2009), 61A, 446–464

TELLUS

Structure and variability of the Filchner overflow plume

By E. DARELIUS[1,2], L. H. SMEDSRUD[2*], S. ØSTERHUS[2], A. FOLDVIK[1] and T. GAMMELSRØD[1], [1]*Geophysical Institute, University of Bergen, Bergen, Norway;* [2]*Bjerknes Centre for Climate Research, Bergen, Norway*

(Manuscript received 24 July 2008; in final form 9 December 2008)

ABSTRACT

Properties of the dense ice shelf water plume emerging from the Filchner Depression in the southwestern Weddell Sea are described, using available current meter records and CTD stations. A mean hydrography, based on more than 300 CTD stations gathered over 25 yr points to a cold, relatively thin and vertically well-defined plume east of the two ridges cross-cutting the continental slope about 60 km from the Filchner sill, whereas the dense bottom layer is warmer, more stratified and much thicker west of these ridges. The data partly confirm the three major pathways suggested earlier and agree with recent theories on topographic steering by submarine ridges. A surprisingly high mesoscale variability in the overflow region is documented and discussed. The variability is to a large extent due to three distinct oscillations (with periods of about 35 h, 3 and 6 d) seen in both temperature and velocity records on the slope. The oscillations are episodic, barotropic and have a horizontal scale of ~20–40 km across the slope. They are partly geographically separated, with the longer period being stronger on the lower part of the slope and the shorter on the upper part of the slope. Energy levels are lower west of the ridges, and in the Filchner Depression. The observations are discussed in relation to existing theories on eddies, commonly generated in plumes, and continental shelf waves.

1. Introduction

Deep water formation at high latitudes is an important part of the thermohaline circulation, and has a central role in discussions of climate change. The Weddell Sea is traditionally thought to be the largest source of bottom water in the Southern Hemisphere (Deacon, 1937; Foldvik and Gammelsrød, 1988; Orsi et al., 1999), although rates and formation areas are a matter of debate (Broecker et al., 1998; Fahrbach et al., 2001; Schlitzer, 2007). The distribution of bottom temperature and oxygen content around Antarctica show, however, that the coldest and most oxygen-rich water has its source in the Weddell Sea region (Deacon, 1937; Orsi and Whitworth, 2004). Part of the deep water 'raw-material' in the Weddell Sea is formed as the ocean interacts with the Filchner–Ronne ice shelf (FRIS) in the southwestern Weddell Sea (see Fig. 1). The water mass, referred to as ice shelf water (ISW), has a temperature lower than the surface freezing point and is formed in the ice shelf cavity as a result of the depression of the freezing point with increasing pressure. The ISW escaping the cavity flows northwards in the Filchner Depression as a subsurface flow. Spilling over the sill, it turns left due to the Earth's rotation, and forms a gravity driven plume on the continental slope (Foldvik et al., 2004). Due to its low temperature, ISW has the potential to sink to the bottom of the Weddell Sea, aided by thermobaricity (Killworth, 1977). While descending the slope, the ISW plume mixes with the overlying Weddell Deep Water (WDW) to form Weddell Sea Bottom Water (WSBW) and eventually Antarctic Bottom Water (AABW).

The plume of ISW exiting from the FRIS through the Filchner Depression was first observed in 1977 by Foldvik et al. (1985a,b). Since then, a number of mooring arrays have been placed on the slope and in the Filchner Depression proper to monitor the flow. The data were synthesized by Foldvik et al. (2004) who estimated the flux of ISW to be 1.6 ± 0.5 Sv, corresponding to a WSBW formation rate of 4.3 ± 1.4 Sv. They further suggested that the ISW plume follows three main pathways down the slope, and that two prominent ridges cross-cutting the shelf slope would influence the path of the cold plume water. This is supported by idealized numerical model runs from the region (Matsumura and Hasumi, 2008; Wang et al., 2008), by laboratory experiments (Darelius, 2008; Wåhlin et al., 2008) and theory (Wåhlin, 2002; Darelius and Wåhlin, 2007).

Greatly simplified, one would expect the dense water spilling over the sill of the Filchner Depression to adjust geostrophically and to flow along the isobaths, with the (upslope) Coriolis

*Corresponding author.
e-mail: lars.smedsrud@gfi.uib.no
DOI: 10.1111/j.1600-0870.2009.00391.x

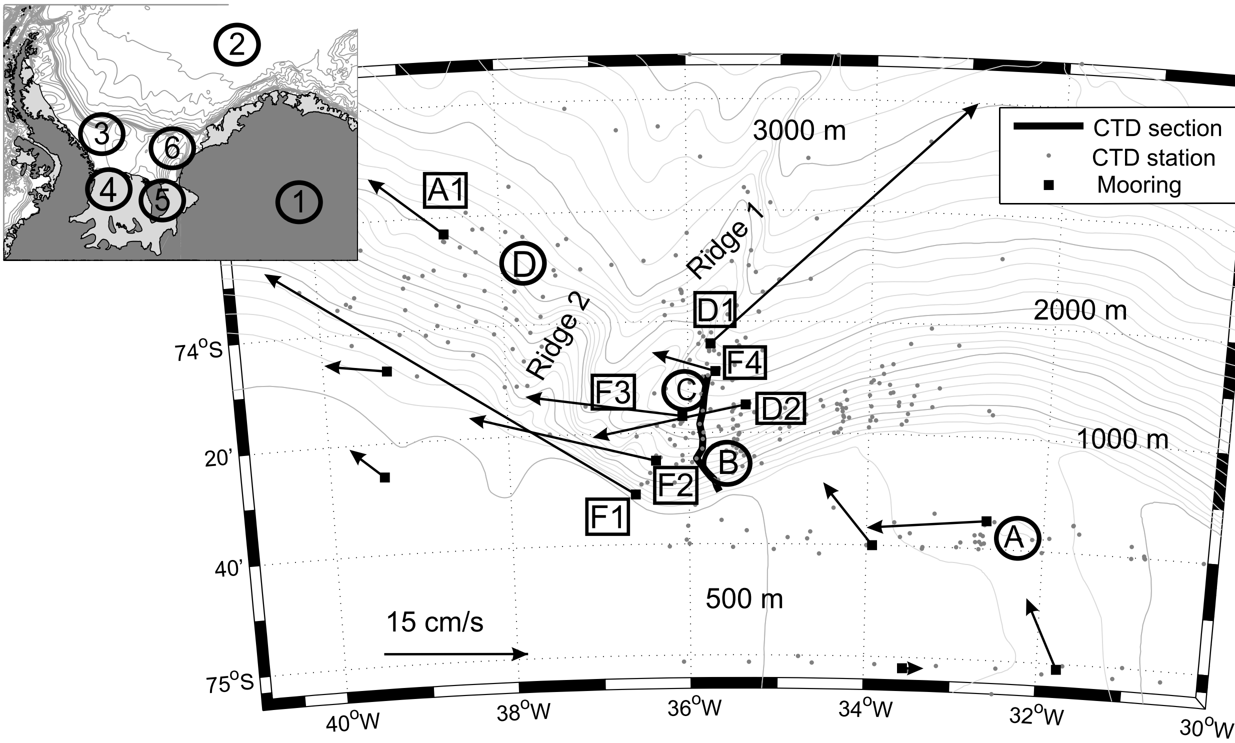

Fig. 1. Map of the study area showing bathymetry and positions of moorings and CTD stations. The arrows indicate the mean current (from Foldvik et al., 2004) at the bottom-most instrument on each mooring. CTD profiles discussed in the text are marked using circles (letters A–D) and moorings using boxes. (1) Antarctica, (2) Weddell Sea, (3) Ronne Depression, (4) Filchner–Ronne ice shelf, (5) Berkner Island, (6) Filchner Depression.

force balancing the (downslope) pressure force. Friction would slow down the flow and cause it to deflect slightly downslope (e.g. Killworth, 2001). Dense fluid would constantly be drained downslope from the lower part of the plume through Ekman drainage (Wåhlin and Walin, 2001). However, most laboratory and model experiments indicate that this picture is too simple, as eddies, waves and subplumes may develop within the plume and greatly alter its shape and velocity patterns (e.g. Smith, 1977; Jiang and Garwood, 1996; Lane-Serff and Baines, 1998; Etling et al., 2000; Cenedese et al., 2004; Ezer, 2006; Wang et al., 2008). Observations from other overflow regions support this (see e.g. Høyer and Quadfasel, 2001; Käse et al., 2003; Geyer et al., 2006 for evidence from the Faroe Bank Channel overflow and Denmark Strait) and it will be shown here that, as suggested by Foldvik et al. (2004), such disturbances probably are generated also within the Filchner overflow. Eddies and waves impact mixing processes (Jiang and Garwood, 1996; Cenedese et al., 2004; Cenedese and Adduce, 2008; Wåhlin et al., 2008) and descent rates (Tanaka and Akitomo, 2001) and they will thus influence the final properties and destiny of the plume water, and consequentially, the properties of the deep water in the oceans.

In this study, the Filchner area and the Filchner plume are revisited. While Foldvik et al. (2004) aimed at providing a transport estimate based on the current meter data, the focus is here on the surprisingly large mesoscale variability. More than 30 yr of field data from CTD and current meter moorings have been synthesized, indicating that a large part of the variability is caused by oscillations at relatively distinct frequencies. The observations are compared with existing theories on overflow and slope variability. Based on the synthesized data, a description of the general plume structure and water properties is given. The pathways suggested by Foldvik et al. (2004) are discussed in relation to the data and recent theories on topographic steering.

2. Data and methods

This work is based primarily on data from 20 current meter moorings that were deployed in the Filchner overflow area between 1968 and 1999. An overview of deployments, instruments and data records is given by Foldvik et al. (2004). Figure 1 shows the position of the moorings and the mean current from the bottom-most instrument at each mooring. A total of 44 current meters (Aanderaa Instruments, models RCM 4/5 and 7/8) were used, recording current (speed and direction) and temperature. The instruments were placed from 10 to 433 m above bottom (mab) and recorded data once every hour. The accuracy for an individual speed and direction measurement is ± 1 cm s^{-1} and $\pm 5^{\circ}$ respectively, according to the manufacturer. For low speeds (<1 cm s^{-1}) systematic errors might occur, but the velocities in the discussed time-series are always well above this threshold.

The record length varies from 15 to 837 d, but is about 1 yr for most instruments. The F1–4 moorings (see Fig. 1) were equipped with Seabird MicroCat (SBE-37) conductivity–temperature sensors in addition to the current meters. These were placed 9 mab, and they have an accuracy of $<0.01\,^{\circ}$C for temperature and <0.004 S m^{-1} for conductivity, according to the manufacturer.

To facilitate comparison between records, the coordinate system at each mooring was rotated to align the x-axis with the isobaths; $u(v)$ is thus directed along (across) the slope. One exemption is mooring D1, which is located in the vicinity of a ridge and for which the direction of the local isobaths is not easily defined. The x-axis is here taken to be aligned with the mean current (see Fig. 1), that is, roughly aligned with the nearby ridge. Moorings in the Filchner Depression have not been rotated.

Fourier analysis was used to identify energy-containing frequencies in the mooring data. Eight Hanning windows with 50% overlap were used in the analysis. The data were not detided prior to the analysis, but tidal frequencies (diurnal and semi-diurnal) are not presented. In addition to 'normal' Fourier analysis on the u and v components of the flow, a rotational Fourier analysis was performed. An oscillation can be divided into a clockwise (CW) and a counter-clockwise (CCW) part, and the analysis identifies energy-containing frequencies in the two rotation directions. In the Southern Hemisphere, a cyclonic (anticyclonic) motion is CW (CCW). It should be noted that it is the rotation of the velocity vector locally that is obtained through this analysis, and not that of the large-scale motion.

Wavelet analysis (Torrence and Compo, 1997) was used to locate episodic oscillations, that is, to show when energy is present at a certain frequency. Prior to the analysis the data were zero-padded and filtered using a 3-h Hanning-filter. The time-series was further analysed using complex demodulation (Emery and Thomson, 2001) to determine the temporal change of the particular frequency components with respect to phase, rotation and orientation of current ellipses. Mean relative phase shift (vertical and horizontal) was obtained from the complex demodulation results and is given as 'mean $\pm$ standard deviation'. Only demodulations that agree well with the original data are included.

In addition to current meter records, CTD data from more than 300 stations collected during a number of years are used. Data from the Norwegian Antarctic Research Expeditions (NARE) are from 1977, 1979, 1980, 1985, 1987, 1989, 1990, 1992, 1993 and 1995. The 1977 and 1979 data were presented in Foldvik et al. (1985a,b) and a few stations from 1990 were presented in Foldvik et al. (2004). CTD data from the Ronne Polynya Experiment (ROPEX) in 1998 (Nicholls et al., 2003), two Alfred Wegener Institute (AWI) cruises in 1986/87 and 1995 (Miller and Oerter, 1990; Wilfried and Oerter, 1997), and data from the World Ocean Circulation Experiment (WOCE) data atlas (Orsi and Whitworth, 2004) have been added to the analysis. The uncertainty in the data generally decreased for more recent cruises, but is assumed to be better than $\pm 0.006\,^{\circ}$C for temperature and ± 0.01 for salinity. Figure 1 shows the positions of the CTD stations, which were all occupied during the Austral summer. When the deepest measurement of the CTD is deeper than the listed echo-depth, the CTD measurement has then been used as the 'true' bottom depth.

The thickness of the plume was determined from the CTD temperature profiles. Above the plume, or when no plume is present, the deeper part of the water column is occupied by WDW with a relatively constant temperature profile, see Fig. 2a. The WDW temperature is close to $0.5\,^{\circ}$C at 1000-m depth and decreases linearly to $0\,^{\circ}$C at 2000-m depth. The thickness of the plume (if present) was defined as the height above the bottom at which the temperature profile deviates from the WDW profile, that is, where the temperature gradient is larger than it is within the WDW (the criteria $\frac{dT}{dz} > 0.5\,^{\circ}$C/100 m was used).

Mean bottom temperature and plume thickness fields were found as follows. The CTD stations in the region between 30°W and 40°W and from depths between 800 and 3200 m were first divided into depth bins of 200 m using the bottom depth recorded at the station, and then into 0.25° bins zonally. The mean bottom temperature and plume thickness were calculated for each depth-longitude bin, and linked to the map using the General Bathymetric Chart of the Oceans (GEBCO; http://www.gebco.net) bathymetry. The GEBCO depth and the depth recorded in the CTD data do not always agree, and the data may then be slightly displaced. Data from the Filchner Depression have not been divided into depth bins but have been projected onto 74°40′S.

3. Results

The CTD data from the Filchner overflow area between 1977 and 1998 are first presented, providing a picture of the mean structure and properties of the plume. It will later be shown that the overflow is highly variable on relatively short temporal and spatial scales, and single CTD casts and sections must thus be thought of as 'snap shots'. No salinity data are presented, as plume water can be distinguished from the ambient WDW based on temperature alone.

3.1. Spatial structure

Before spilling over the sill, the ISW is found as a northward flowing subsurface layer in the Filchner Depression (Foldvik et al., 2004). The ISW is stratified by salinity, which increases towards the bottom to a salinity between 34.6 and 34.7. A typical temperature profile from the Filchner Depression is presented in Fig. 2a (profile A, see Fig. 1 for location), where the surface freezing point ($T_f \sim -1.9\,^{\circ}$C) is marked. ISW, or water with temperatures lower than $-1.9\,^{\circ}$C, is found below about 500-m depth. The minimum bottom temperature recorded in the Filchner Depression is $-2.22\,^{\circ}$C.

When spilling over the sill, the ISW forms a dense plume that mixes with and entrains ambient WDW as it flows along the

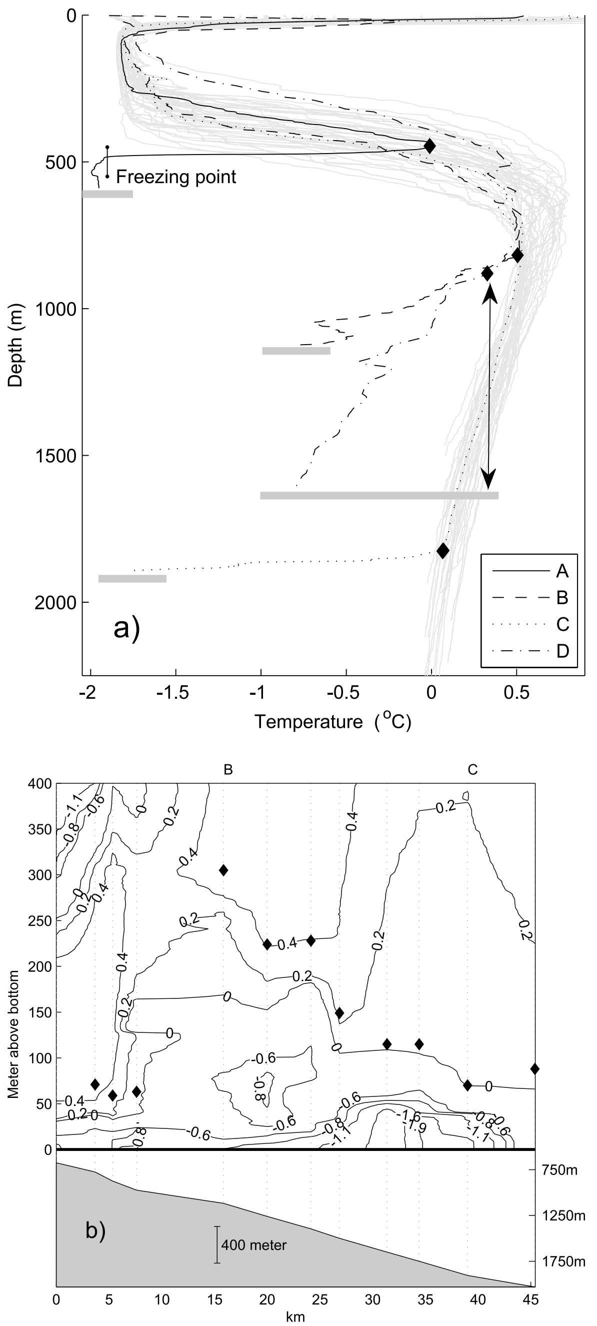

Fig. 2. Temperature profiles and sections from the Filchner overflow, see Fig. 1 for location. (a) Temperature profiles A–C from NARE 1985 (stations 13,80, 86), and profile D from Glacier 1978 (station 74). Black diamonds indicate height of the plume and the arrow indicates the plume thickness for profile D. The bottom for each profile is marked with a horizontal grey line. Background WDW profiles (from NARE 1985, 1987 and ROPEX 1998) are included as thin grey thin lines, where data influenced by plume water have been removed. (b) Temperature section from NARE 15 February 1985 showing the deepest 400 m. Dotted lines indicate stations, and profiles B and C shown in (a) are marked. The lower panel shows the corresponding bottom topography.

slope. Figure 2a shows three characteristic temperature profiles from the slope (profiles B–D, see Fig. 1 for location), illustrating the 'evolution' of the cold bottom plume layer. Profile C shows a thin, cold bottom layer, while profiles B and D show thicker layers with a higher minimum temperature. Profiles from the area west of the ridges are generally similar to profile D, whereas those east of the ridges are more similar to C. The eastern (western) ridge will hereafter be referred to as Ridge 1 (Ridge 2), see Fig. 1.

The thickness of the plume, defined as the height at which the temperature profile deviates from the background WDW profile, is indicated in Fig. 2 by black diamonds. The maximum plume thickness observed on the slope is 860 m. Stations that have a bottom temperature close to the freezing point generally have a plume thickness below 300 m, but mooring data occasionally show low temperatures at shallower depths (e.g. 433 mab at mooring F2). The bottom temperature of the thickest plume layers is usually in the range -1.0 to $-0.5\,^{\circ}$C.

Figure 2b shows a temperature section obtained 15 February 1985. The section crosses the slope from 600- to 2000-m depth and runs parallel to Ridge 1 along 36°W (see Fig. 1 for location). Only data from the bottom-most 400 m are shown. A main cold core of the plume is visible around 1700-m depth (35 km) where the bottom temperature is $-1.91\,^{\circ}$C and the plume thickness about 120 m (profile C). Higher up on the slope the bottom layer has a larger vertical extent (~300 m), and a higher minimum temperature (profile B). The interval between the occupation of the first and the last station is 14 h, and it is uncertain to what level the 'snap-shot' is influenced by temporal variability (compare, e.g. with the yo-yo-station discussed later, Fig. 5, which was occupied during 20 h).

The 'mean' bottom temperature (from CTD and mooring data) and plume thickness are shown in Fig. 3. The background WDW temperature is $0\,^{\circ}$C at 2000-m depth, and $-0.15\,^{\circ}$C at 3000-m depth. A near-constant layer of ISW is seen in the Filchner Depression (west of 31°W along 74°40′S), where the bottom temperature is below $-1.9\,^{\circ}$C and the layer thickness about 200 m. Stations on the slope with a cold bottom layer are usually found west of 33°30′W. As expected, the bottom temperature generally increases towards the north (deeper waters) and west (Fig. 3a), and the plume thickness increases (Fig. 3b). The core of the cold plume at ~1000-m depth can be found around 34°W (Fig. 3a), but low bottom temperatures are also found further west. The plume flows west while sinking down, and west of 35°W, the plume is found around 2000-m depth. As the plume advances, it encounters Ridge 1, and Fig. 3a shows that low bottom temperatures and small layer thicknesses are found in the vicinity of Ridge 1 at relatively large depths. The minimum bottom temperature observed with CTD in this region is $-1.64\,^{\circ}$C at 2175-m depth, while mooring D1 at 2100-m depth recorded a minimum temperature of $-1.92\,^{\circ}$C. Eight percent of the data points from the lowest instrument at D1 (25 mab) are below $-1.64\,^{\circ}$C. West of Ridge 2, (diluted) plume water occupies most

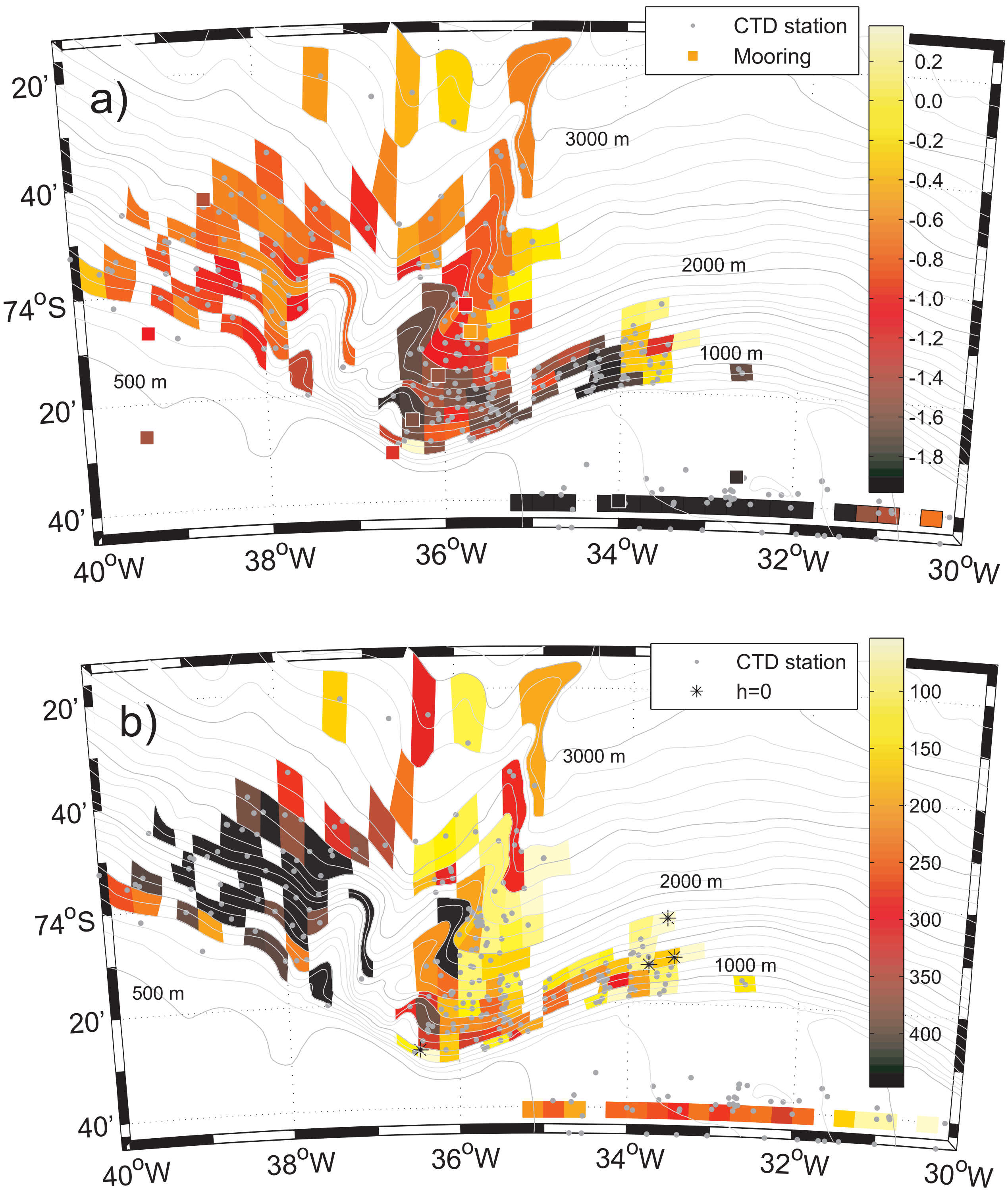

Fig. 3. Mean (a) bottom temperature and (b) plume thickness from CTD stations in the Filchner overflow area. Small, grey dots indicate the positions of individual CTD stations. The colour shading represents calculated means over depth ranges of 200 m (i.e. 800–1000, 1000–1200, . . . , 3000–3200) and in 0.25° longitude bins (i.e. 30°W–30.25°W, 30.25°W–30.50°W, . . . , 39.75°W–40.00°W). In (a), moorings are shown as squares, with their colour indicating the recorded mean bottom temperature. The plume thickness in (b) is found using the vertical temperature profiles as illustrated in Fig. 2. Values smaller (larger) than 50 (450) m are indicated as 50 (450) m. Stations where no plume was observed are marked with an asterisk.

of the slope between 800- and 2500-m depth. The temperatures are higher than east of Ridge 1; around $-1\,^{\circ}$C at 1500-m depth and $-0.5\,^{\circ}$C at 2500 m, and the plume considerably thicker; 400 m or more. No thin cold stations, such as profile B in Fig. 2a, are found west of Ridge 2. The coldest moorings are F2 and F3 at 1200- and 1700-m depth close to 36°W (see Fig. 1 for location). They have mean temperatures around $-1.6\,^{\circ}$C, which is close to the mean value from the CTD stations.

3.2. *Variability*

The current meter records reveal a surprisingly large temporal variability in the area. It will here be shown that a large part of the variability is due to oscillations at more or less distinct frequencies. The tides, which are strong in the area, have been discussed elsewhere (Middleton et al., 1987; Foldvik et al., 1990), and the focus is here on the oscillations with periods of 35 h, 3 and 6 d that are repeatedly found in the mooring records. The oscillations will first be shown as they appear on individual moorings, before their geographical and temporal distributions are presented.

3.2.1. The 35-h oscillation. A 35-h oscillation can be observed, for example, in the temperature and velocity records at mooring F2, which was located in the centre of the plume path at 1180-m depth and recorded at four levels; 10, 56, 202 and 433 mab. The mean thickness of the plume in this area is 250–300 m (Fig. 3b). Temperature and velocity records from the mooring during a period when the oscillation is present are shown in Fig. 4. The temperature (Fig. 4a) at the shallowest instrument, which is usually above the plume and surrounded by WDW at 0.5°, oscillates with a period of about 35 h and is seen to drop below $-1.5\,^{\circ}$C. Meanwhile, the temperature at the deepest instrument oscillates between -2.0 *and* $0.0\,^{\circ}$C, that is, the mooring is surrounded alternatingly by ISW and WDW. The 35-h oscillation is evident in the velocity data (Fig. 4b), where the oscillation in the along-slope component lags the across-slope component, giving a CW rotation locally. The amplitude of the oscillation is 10 cm s^{-1}, and the signal is seen, unattenuated, at all depths. The vertical phase shift is not significantly different from zero (see Table 1).

During this period, an oscillation with the same period is observed at F1 (not shown), located further up the slope at 647-m depth. Here, the temperature at all instrument depths (10, 100, 207 mab) oscillates between -1.8 *and* $0.5\,^{\circ}$C. The amplitude of the velocity oscillation is smaller than at the deeper F2, but the signal is again almost vertically homogeneous with no significant vertical phase shift (Table 1). Contrary to F2, the along-slope component leads, and the motion is CCW.

The difference in along-slope velocity between moorings can be used as a proxy for relative vorticity (i.e. $\zeta = v_x - u_y \sim -u_y \sim -\Delta u/\Delta y$). During the period shown in Fig. 4, the vorticity is oscillating between positive and negative values, where negative (positive) vorticity is co-occurrent with low (high) bottom temperatures at both moorings. This relation is not, however, always clear or consistent during other periods of 35-h oscillation at these moorings.

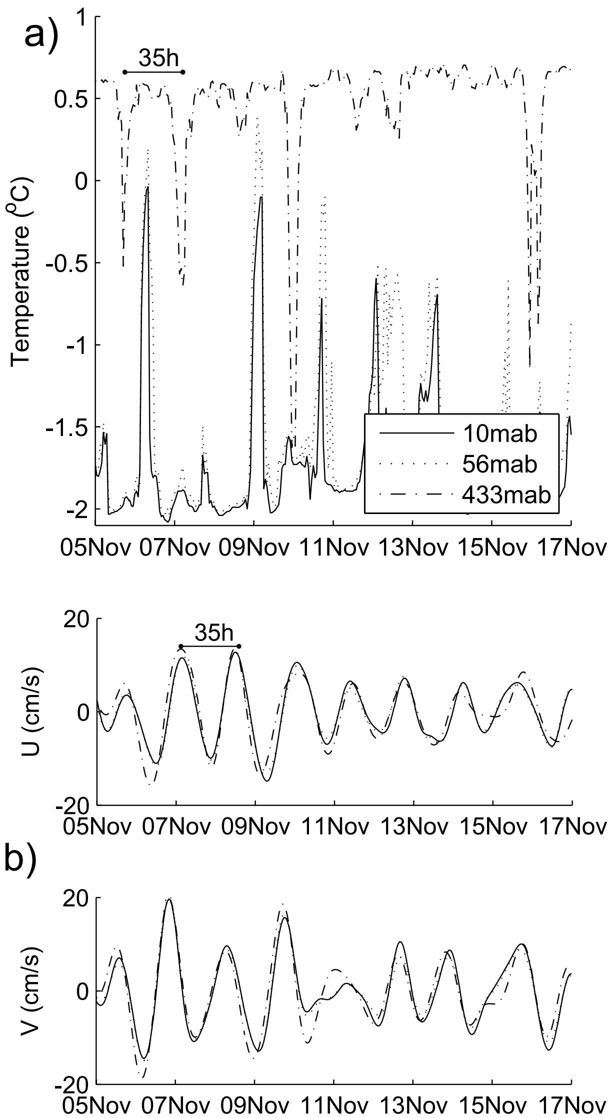

Fig. 4. (a) Temperature and (b) velocity from F2 (1180-m depth) in November 1998 showing a 35-h oscillation. The instrument at 202 m was not operating during the period shown. The records have been filtered (band passed 24-72 h). The key in (a) applies to both graphs.

Somewhat fortunately, a 35-h oscillation was documented by a CTD yo-yo-station occupied in the vicinity of F1 just after the mooring was deployed. The temperature profiles are shown in Fig. 5a, and the deviation from the mean profile (shown in black in Fig. 5a) is shown in Fig. 5b as a function of time. It is evident that the properties of the whole lower part of the water column (below about 300-m depth) changes drastically during the 20 h that the station was occupied, and that the changes are directly related to the velocity oscillation observed at the

Table 1. Relative phase shift at moorings F1, F2, F3 and F4 for the different oscillations

	O35		O3		O6	
	$\Delta\Phi_u$	$\Delta\Phi_v$	$\Delta\Phi_u$	$\Delta\Phi_v$	$\Delta\Phi_u$	$\Delta\Phi_v$
F1–2	$115° \pm 36°$	$-33° \pm 23°$				
F2–3	$73° \pm 38°$		$102° \pm 36°$	$-35° \pm 64°$		
F3–4					$110° \pm 33°$	
F1	$2° \pm 9°$	$-4° \pm 11°$				
F2	$2° \pm 8°$	$1° \pm 6°$	$1° \pm 6°$	$5° \pm 9°$		
F3			$38° \pm 18°$	$20° \pm 13°$		
F4					$1° \pm 8°$	$3° \pm 6°$

Note: Horizontal phase shift is between moorings, and vertical phase shift is between instruments at one mooring. Values are given as mean ± *SD*. Positive values indicate that the shallower mooring/instrument leads.

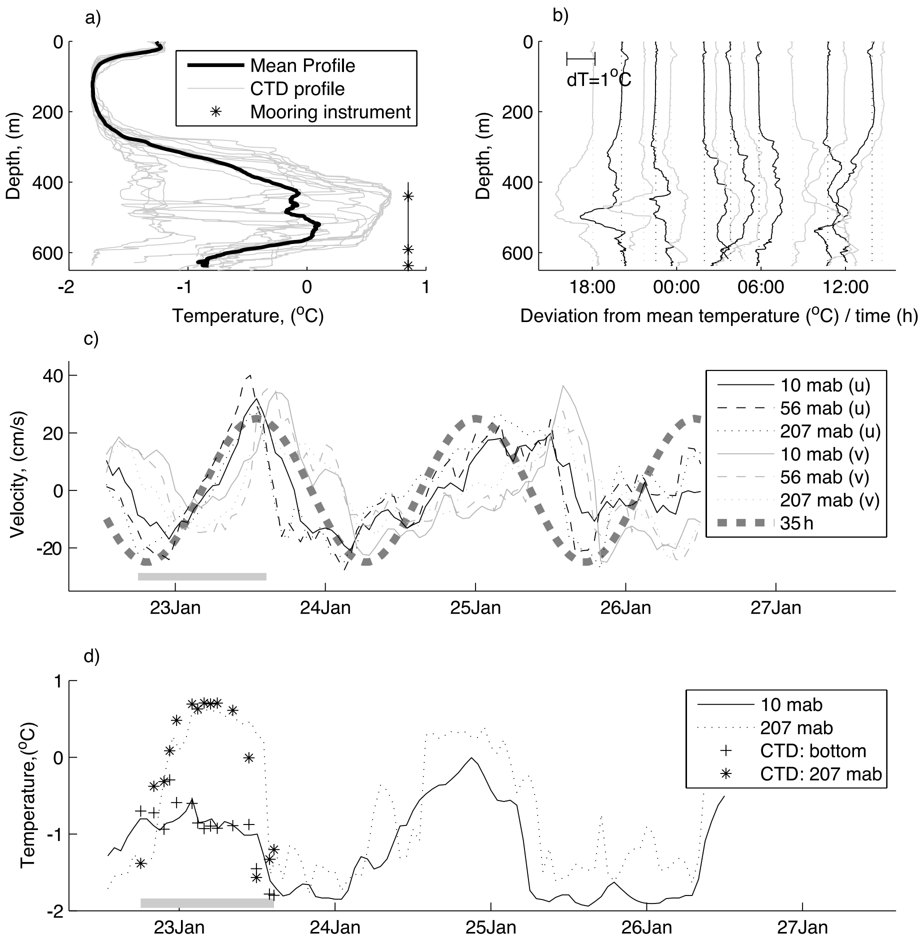

Fig. 5. (a) Temperature profiles from a repeated CTD station occupied in the vicinity of mooring F1 (see Fig. 1) between 22 January (18:00 UTM) and 23 January (14:30 UTM) 1998. The depth of the instruments at the nearby F1 mooring is indicated with asterisks. (b) Deviation from the mean temperature profile shown in (a) over time. The dashed vertical lines show zero deviation and their placements on the *x*-axis indicate when the stations were occupied. (c) Currents from the three instruments at F1 between 22 and 26 January 1998. The period during which the nearby yo-yo-station was occupied is marked in light grey. A 35-h sinusoidal oscillation is super-positioned. (d) Temperature at the bottom and 207 mab from the CTD yo-yo-station and F1.

mooring (Fig. 5c). The vertical pattern is complicated, with the largest temperature variations (during the yo-yo-period) occurring at 400–550-m depth. The cold intrusions at around 450 m depth are not plume water, but slightly fresher, cold water probably originating from the shelf. Later on, after the occupation of the yo-yo-station, the amplitude of the temperature oscillation is large also at the bottom (Fig. 5d). The horizontal excursion due to the oscillation is about 5 km.

3.2.2. The 3 and 6-d oscillation. Oscillations, similar to those described above but with periods of 3 and 6 d are observed on the slope, for example, at F3, F4 and D1 (see Appendix A1 and A2, where the observations at these moorings are described in further detail). Like the 35-h oscillation, the oscillations are observed in both temperature and velocity. At shallow instruments, never submerged in plume water, a small-amplitude oscillation ($\sim$0.1 °C) is often observed, which is out of phase with the oscillation recorded at depths within the plume. That is, when the deeper instruments are surrounded by cold plume water, the temperature at the shallow instrument increases. The temperature gradient in the overlying WDW is about $0.5\,^{\circ}\mathrm{mC\,m^{-1}}$, and a temperature difference of 0.1° corresponds to a vertical excursion of about 200 m.

At mooring D1, where a strong 6-d oscillation is apparent, the oscillatory motion is aligned with Ridge 1.

3.2.3. Oscillations on the slope. Fourier analysis reveals that the three oscillations introduced above and henceforth referred to as O35 (35 h), O3 (3 d) and O6 (6 d), are relatively energetic and reoccur over the slope. The periods are (within the accuracy of the methods used) multiples of each other: O6 = 2 × O3 = 4 × O35. Figure 6 shows the Fourier spectra for four instruments on the slope. Some moorings have pronounced peaks (i.e. energy) at all three frequencies (e.g. F3, Fig. 6a) while others have one (e.g. D1, Fig. 6b) or two (e.g. D2/F2, Figs. 6c and d) dominant peaks. At some moorings, the peaks are seen in both velocity components (e.g. F2, Fig. 6d), while one component is totally dominant at others (e.g. *u* at D1, Fig. 6b). At D2, O35 is strongest in the along-shelf component and O3 in the across-shelf component. The division of the energy between CW and CCW motion is included in Fig. 6. In general, the oscillation is CCW at the shallower of the moorings where it is observed, and CW at the deeper. The observation of a CCW motion O35 at D2 (Fig. 6c) is, however, an exemption. The shallow moorings west of Ridge 2 have low energy levels and no prominent peaks, other than at tidal frequencies, while O6 is observed at mooring A1 at 1939-m depth (not shown).

Figure 7 gives an overview of the energy levels at the three frequencies (O35, O3 and O6) at the moorings. Energy levels are highest in the area between the Filchner Depression and Ridge 1,

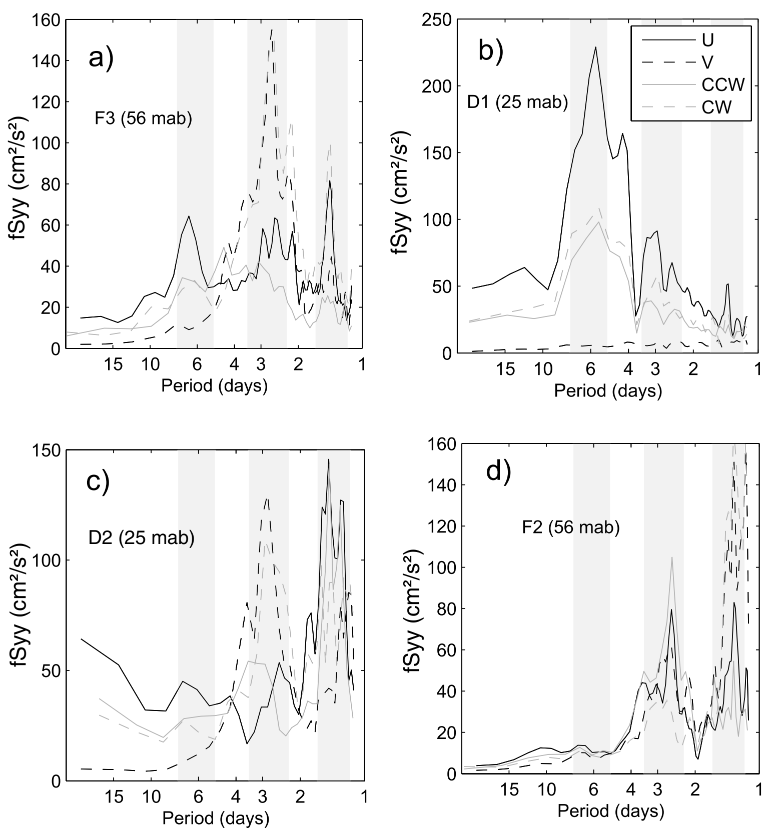

Fig. 6. Fourier and rotary spectra for mooring (a) F3 (56 mab), (b) D1 (25 mab), (c) D2 (25 mab) and (d) F2 (56 mab). The legend in (b) is valid for all graphs. The shaded areas indicate the frequency intervals included in Fig. 7.

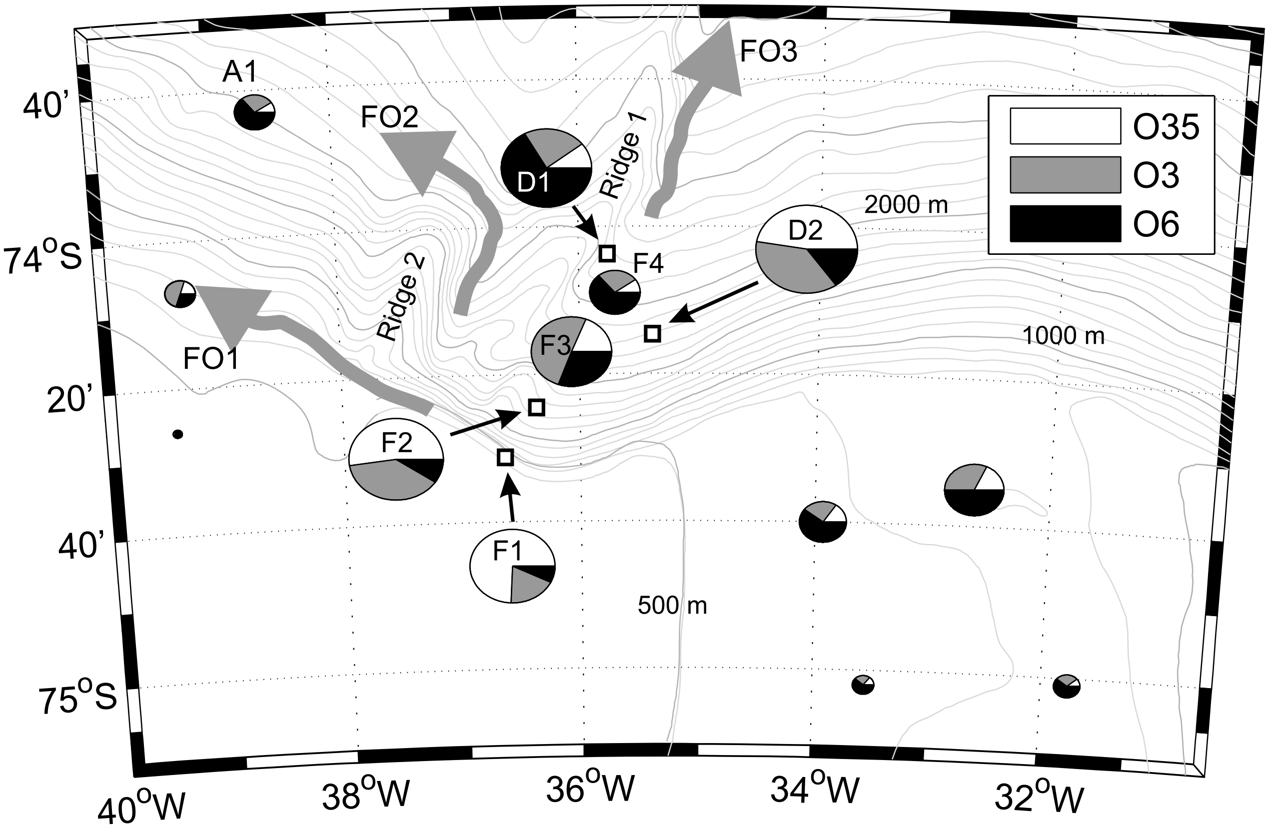

Fig. 7. Partition of energy between O35, O3 and O6. Each mooring is represented by a pie-chart whose area is proportional to the total mean energy level of the three frequencies and where the distribution of the energy amongst them is indicated by the size of the sector. The energy level is calculated as the mean over an interval $f \pm \Delta f$ (shaded grey in Fig. 6) around the frequencies of interest. Velocity data from all instrument levels on the moorings have been included. The light grey arrows (FO1–3) are the pathways suggested by Foldvik et al. (2004) and discussed in Section 4.1.

while lower levels are found in the depression and west of Ridge 2. There is a tendency for the shortest period (O35) to be more pronounced at the upper part of the slope, while the longest (O6) is more energetic further down and the intermediate (O3) in the middle part of the slope. Mooring D2 is however, again, an (energetic) exception. The moorings in the Filchner Depression have high energy levels at longer periods (10–15 d), but of the three frequencies discussed here only O6 is observed.

Figures 8a–c show the co-occurrence of the oscillations and the orientation of the current ellipses at the moorings F1–4, while Table 1 lists the relative phase difference. The shallow moorings leads in u and lags in v, in agreement with the general picture of CCW motion at the shallow moorings and CW motion at the deeper moorings.

3.2.4. Temporal distribution. The episodic nature of the oscillations at most of the moorings and their persistency at others become apparent through wavelet analysis. Figure 9 presents results from the wavelet analysis of records from moorings D1 and D2, placed 24 km apart at a depth of 2100 and 1800 m, respectively (during 1985). The differences between the two moorings are striking. D1 shows a relatively persistent 6-d oscillation in u, here directed along the mean current/Ridge 1 (Fig. 9a), while D2 (Figs. 9b–c) shows an intermittent 35-h oscillation in the along-slope velocity (u) and a more persistent tidal (diurnal) and 3-d oscillation in the across-slope velocity (v). The strength of, for example, O35 at D2 (Fig. 9b) appears to be modulated with a period of about 14 d. A similar modulation, with a period of roughly 14 d, seems to be present, for example, in O3 at F3, and in O35/O3 at F2 (not shown).

The 35-h oscillation (in u) at D2 brings plume water ($\sim -1.9\,^{\circ}$C) to the mooring, which in periods without the oscillation is surrounded by WDW ($\sim 0\,^{\circ}$C). The correlation between u and T at D2 is high (r = 0.85), with high (50–75 cm s^{-1}) westward velocities at low temperatures (see also Foldvik et al., 2004, fig. 12, section 6.2). The cold water is thus advected along the slope, and not across it. The co-occurrence of low temperatures and oscillations is apparent at other moorings located at the lower (F4—O6) and upper (F1—O35) sides of the plume. It is notable that the strong, predominantly diurnal tidal signal (in both u and v) at F1 (close to the shelf break) is apparent in the velocity records but not in the temperature records, while O35 affects both velocity and temperature.

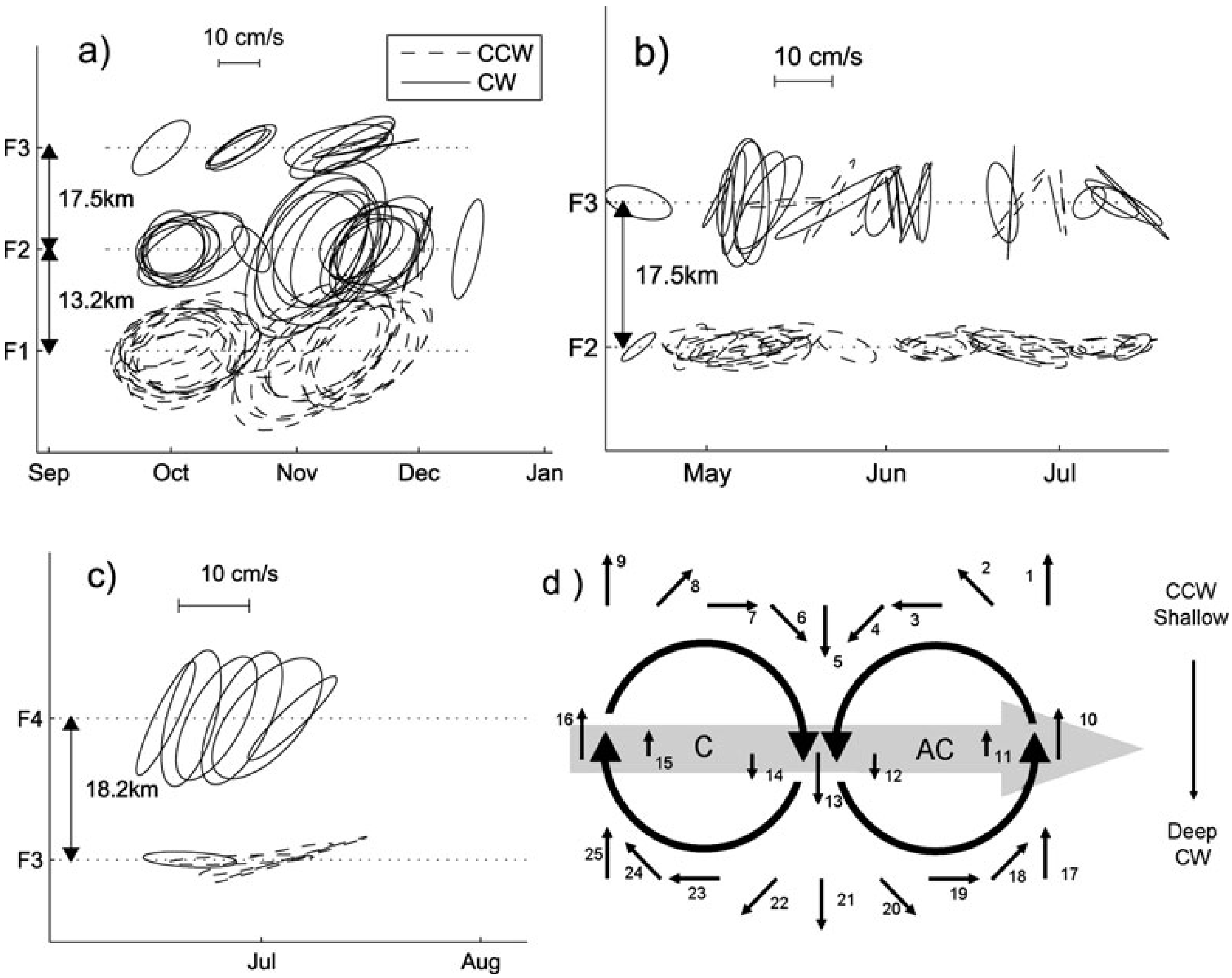

Fig. 8. (a) O35, (b) O3 and (c) O6 current ellipses from complex demodulation. Only ellipses that correlates ($r > 0.7$) with the original data is shown. (d) Sketch of a cyclonic (C) and an anticyclonic (AC) eddy translating towards the right-hand side on a slope, causing a CCW (CW) motion locally on the upper (lower) part of the slope and an across-slope oscillation in the centre. The grey arrow indicates the direction of eddy translation, the thick black arrow indicates the rotation of the eddy and the small, numerated black arrows indicate the currents registered at moorings located on the shallow side (arrows 1–9), in the centre (arrows 10–16) and on the deep side (arrows 17–25) of the eddies.

3.2.5. Summary. The current meter records from the Filchner area show that oscillations with periods of about 35 h (O35), 3 d (O3) and 6 d (O6) are present, in addition to tidal motion. These periods are observed at several locations, and in records from different years. The observations are summarized below and in Table 2.

(1) Oscillations in velocity are accompanied by oscillations in temperature.

(2) Velocity amplitudes range from 5 to 35 cm s^{-1}.

(3) The oscillatory motion is neither attenuated nor strengthened with depth. This is apparent also when the shallowest instruments are above the dense bottom layer, and the motion is thus barotropic or close to barotropic.

(4) There is no significant vertical phase shift, with the exemption of O3 at F3, where the velocity leads at the shallower instrument.

(5) The (small) temperature oscillations ($\simeq 0.1\,^{\circ}$C) recorded at instruments above the plume (surrounded by WDW) are often out of phase with the (larger) temperature oscillations at the lower instruments.

(6) The oscillations are (with a few exceptions) episodic and on a number of moorings the oscillations are associated with the presence of cold plume water at the mooring.

(7) The strength of the oscillations (O35, O3) appears on some moorings to be modulated with a period of about 14 d.

(8) Both CW and CCW motions are observed, with CCW motion generally located higher up the slope.

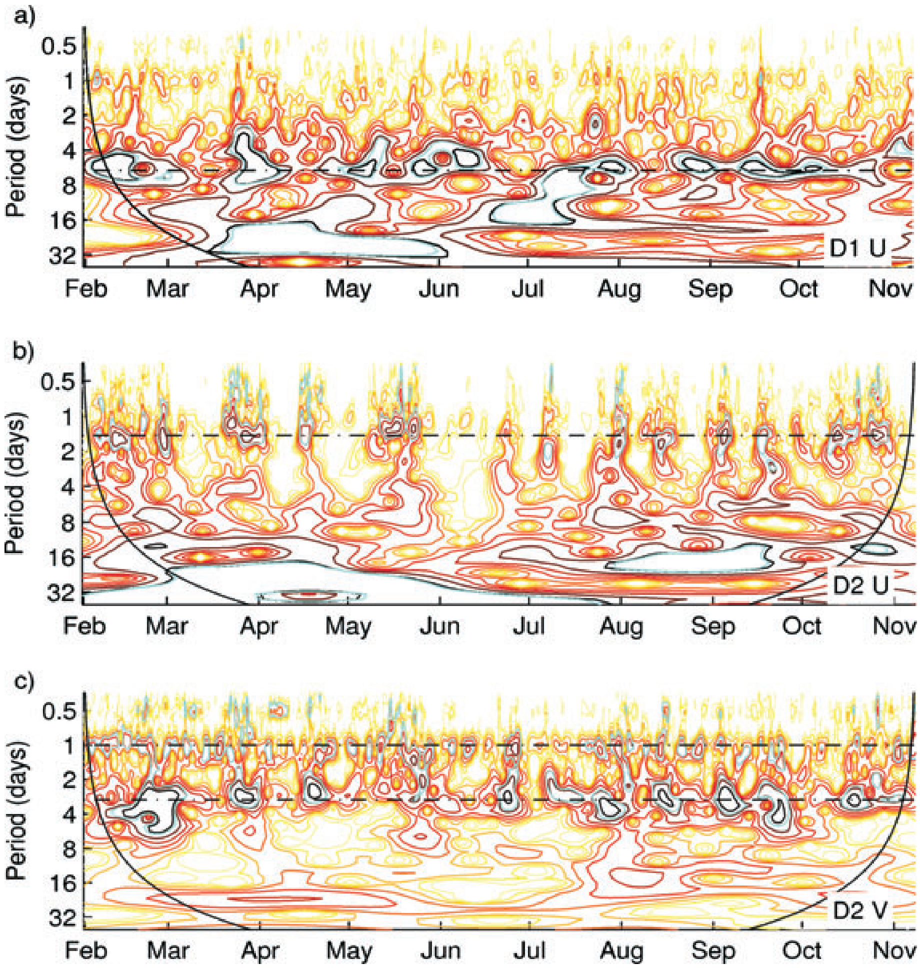

Fig. 9. Results from wavelet analysis for moorings (a) D1 (25 mab) along-ridge velocity (u), (b) D2 (25 mab) along-slope velocity (u) and (c) D2 (25 mab) across-slope velocity (v). Dark (brown) contours indicate high energy levels and light (yellow) low levels. The blue contours are 95% confidence levels. Black contours mark the 'cone of influence', that is, where end-effects are expected. Frequencies discussed in the text are marked with dashed lines.

(9) The shortest period (O35) is generally stronger on the upper part of the slope, while O6 is observed at the lower part and O3 in between.

(10) Moorings in the Filchner Depression, on the continental shelf and west of the two ridges have relatively low energy levels and no distinct peaks at O35 and O3, while O6 is discernible in the depression and at the deep, western mooring (A1).

4. Discussion

4.1. Structure

The ~25 yr of CTD data presented in Section 3.1 confirm the presence of a cold bottom plume westward of 34°W and deeper than 800 m (data from the shallower part of the slope have not been included in the analysis). Bottom temperatures and plume thickness increase westward, as expected, but there is a qualitative difference between CTD profiles east and west of the two ridges, suggesting that the transition is not gradual. CTD casts from locations east of Ridge 1 often show low temperatures and thin plumes with large temperature gradients, indicating that mixing and entrainment of ambient WDW is relatively low – or at least intermittent – in the sill region and the first part of the slope. West of Ridge 2, the plume is thick (>400 m), and it has relatively high bottom temperatures and small vertical temperature gradients. There is hence qualitative evidence for vigorous mixing and entrainment in the ridge region. No attempts to quantify mixing rates have been made, however, since the high temporal variability makes budget estimations questionable. The idealized numerical simulations by Wang et al. (2008) also show an increase in layer thickness and temperature – and hence intensive mixing – across the ridge region, albeit much less dramatic than in the observations.

Table 2. Summary of observations of oscillations (O35, O3 and O6) at the moorings

	Observed at	Water depth (m)	U	V	T	CCW/CW	Comments
O35	F1	647	x	x	x	CCW	Episodic, v. homogenous
	F2	1180	(x)	x	x	CW	Episodic, v. homogenous
	F3	1637	x	(x)	x	CW	Episodic, not v. homogenous (shallow instrument leads)
	D2	1800	x		x	-	Episodic, co-occurrent with low temperatures cold/warm water flowing west/eastwards
O3	F2	1180	x	x	(x)	CCW	Episodic, v. homogenous
	F3	1637	(x)	x	x	CW	Relatively persistent, v. homogenous
	D2	1800		x		-	Relatively persistent
	F4	1980	(x)	(x)	x	CW	Episodic
O6	F.D.	∼600	(x)	(x)		CCW	Energy also at lower frequencies
	F3	1637	x			-	Episodic, v. homogenous
	A1	1939	(x)	(x)			
	F4	1980	x	x	x	CW	Episodic, co-occurrent with low temperatures, v. homogenous cold/warm water flowing northeast/southwestwards
	D1	2100	x		x	-	Persistent, cold/warm water flowing downslope/being stagnant

Note: F.D., Filchner Depression; v., vertical and '(x)' means that the oscillation is observed, but that the energy level is relatively low.

Ridges (and canyons) can potentially steer all or portions of a dense plume downslope, and it has been suggested that this process is of importance to the Filchner plume (Darelius and Wåhlin, 2007). The two prominent ridges cross-cutting the plume path could in fact cause the division suggested by Foldvik et al. (2004), see Fig. 7. Given the dimension of a canyon or ridge cross-cutting a slope their transport capacity, that is, the maximum amount of dense water that they can steer downslope, may be calculated (Wåhlin, 2002; Darelius and Wåhlin, 2007). The transport capacity of Ridge 1 has been estimated to 0.3 Sv (Darelius and Wåhlin, 2007), while that of Ridge 2 can be estimated to 0.6 Sv (using a ridge width/height, $W = 7$ km$/H = 500$ m, an Ekman layer thickness, $\delta = 35$ m, a bottom slope, $s = 0.03$, and an idealized cosine shaped canyon). The values can be compared to the total outflow of 1.6 ± 0.5 Sv ISW (Foldvik et al., 2004), and it is evident that the ridges have the potential to channel a substantial part of the overflow downslope. The estimated fluxes and the transport capacities are summarized in Table 3. If the plume transport is larger than the transport capacity of a ridge crossing its path, it is anticipated that the flow will split, with one branch flowing over the ridge, continuing westwards along the slope and one flowing downslope along the ridge, as observed in Darelius (2008). In the Filchner region, one would hence expect one part of the plume to be steered downslope by Ridge 1, one part to be steered by Ridge 2 while the remaining dense water continues along the slope. This picture agrees well with the three major pathways of the Filchner overflow (FO1, FO2 and FO3, see Fig. 7) that were proposed by Foldvik et al. (2004), based on CTD and current meter data. FO3 would hence be the branch steered by Ridge 1, FO2 the branch steered by Ridge 2, continuing along the slope as Ridge 2 ends at about 2000-m depth, and FO1 would consist of the dense water escaping topographic steering. A similar division of the plume is observed in idealized model simulations from the region (Matsumura and Hasumi, 2008; Wang et al., 2008).

The existence of FO3 is supported by the synthesized data; it can be seen in the mean temperature and thickness fields (Fig. 3) and it is evident from the current measurements at D1

Table 3. Estimated transports (from data) and calculated transport capacities for Ridges 1 and 2

	Filchner overflow (ISW)	End product 4000m (WSDW)	Ridge 1 FO1	Ridge 2 FO2
Estimated transport	1.6 ± 0.5[a]	4.3 ± 1.4[a]	0.2[a]	
Transport capacity ($\Delta\rho = 0.1$)			0.3[b]	0.6
Transport capacity ($\Delta\rho = 0.05$)			0.15	0.3

Note: The transports are given in Sverdrups (1 Sv = 10^6 m^3 s^{-1}).
[a]From FO4.
[b]From Darelius and Wåhlin (2007).

that the cold water is flowing downslope, along the ridge. FO3 is discussed in more detail in Darelius and Wåhlin (2007), and the transport along this path was estimated (based on the D1 mooring) to 0.2 Sv by Foldvik et al. (2004). Contrary to the results by Wåhlin et al. (2008), who showed that mixing was enhanced in a topographically steered flow, the plume water flowing along Ridge 1 and past mooring D1 is relatively cold and undiluted.

Foldvik et al. (2004) based the existence of FO2 on mooring A1 at 2000-m depth, deployed in 1978 and on CTD data from 1973 (Foster and Carmack, 1976), which were not available for the current study. The mean flow at mooring A1 is directed along the slope (Fig. 1). The mooring had a mean temperature of -1.3 (-1.2) °C at 25 (125) mab, with very low variability (the standard deviation is 0.1 °C, compared with 0.5 °C at D1, which is at roughly the same depth). The CTD data collected directly east of the mooring (mostly from 1978), indicate higher bottom temperatures (~ -0.8 °C), and more or less uniform temperatures across the slope west of Ridge 2. There is hence no trace of FO2 in the synthesized CTD data, and an apparent contradiction between the CTD data and the results from mooring A1. This may have a trivial explanation—while the CTD sonde was run all the way to the bottom during the NARE expeditions, it is possible that it have been stopped (not to destroy the sonde) well above the bottom in other expeditions (especially in the old expeditions, when they were not 'looking' for a bottom plume). Thus, there may well be a colder layer – and a well-defined FO2 – below the overall thicker warmer layers evident in Fig. 3, as suggested by mooring A1 and Foldvik et al. (2004). The region between the ridges is heavily undersampled – with just one CTD station at about 1500 m – and the presence of a topographically steered plume, leaning on Ridge 2, can thus be neither verified nor dismissed. The one CTD station does, however, show a cold bottom layer (minimum temperature -0.8 °C), with a thickness roughly equal to the height of Ridge 2 (600 m).

The upper pathway, FO1, which was suggested by Foldvik et al. (2004) to follow the continental slope westward at 600–800-m depth is too shallow to be detected in the analysis.

The transport capacities of Ridges 1 and 2 stated above and listed in Table 3 refer to a density difference of 0.1 kg m^{-3} between the plume water and the ambient water. If the density difference is reduced by, let us say a factor two due to entrainment (ambient stratification and the thermobaric effect will also affect the density difference), then so is the transport capacity. At the same time, the volume flux of the plume doubles. A topographically steered, entraining plume must hence be expected to continuously spill over the ridge (or canyon) on which it is leaning. The outflow of 1.6 Sv ISW from the Filchner Depression corresponds to, after entrainment of WDW during its descent, about 4.3 Sv of WSBW (Foldvik et al., 2004) found below 4000 m. Between the sill and 4000 m the volume flux thus increases with a factor of about 2.7, and the transport capacity of Ridges 1 and 2 will decrease accordingly. The relatively thick layer of 'diluted' plume water west of Ridge 2 agrees qualitatively with the picture of a topographically steered, entraining plume spilling over the ridge, but it is questionable if it does so quantitatively.

4.2. Variability

The energetic oscillations in the overflow area described in Section 3.2 (O35, O3 and O6) could be caused by external disturbances such as waves travelling into the area, or be generated locally and then most likely directly related to the overflow. Observations from other overflows (Bruce, 1995; Girton and Sanford, 2003; Geyer et al., 2006), laboratory experiments (Smith, 1977; Lane-Serff and Baines, 1998; Etling et al., 2000; Cenedese et al., 2004) and numerical models (Tanaka and Akitomo, 2001; Ezer, 2006; Wang et al., 2008) show that eddies and waves may form within dense overflows and plumes. One external candidate is continental shelf waves (CSW), which would travel westwards along the shelf. Shelf waves cause the enhanced diurnal tides observed at the shelf break (Middleton et al., 1987; Robertson, 2005), and were mentioned by Foldvik et al. (2004) in connection with the 3–6-d oscillations. Both eddies and shelf waves will be discussed below.

4.2.1. Eddies. Eddies are generally thought to form in dense overflows and plumes either through vortex stretching (Lane-Serff and Baines, 1998; Spall and Price, 1998) or baroclinic instability (Smith, 1976; Swaters, 1991; Jiang and Garwood, 1996; Tanaka and Akitomo, 2001). Vortex stretching tends to form strong eddies close to the source, while baroclinic instabilities form during establishment of an along-slope flow (Lane-Serff, 2001). The baroclinic eddies are often accompanied by subplumes, such as in laboratory experiments by Etling et al. (2000). Both generation mechanisms will be considered here.

Spall and Price (1998) discussed 'baroclinic instabilities' in relation to the Denmark Strait overflow, and concluded that the observed eddies probably were not generated by such instabilities. Many of their arguments can be applied to the Filchner overflow. The oscillations observed in the Filchner overflow show little or no vertical phase shift (with the exception of O3 at F3), while growing baroclinic waves require a substantial shift. Contrary to the observed barotropic (or close to barotropic) oscillations, eddies formed from baroclinic instabilities are stronger within the dense bottom layer than in the fluid above. The baroclinic eddies are concentrated, or at least much stronger, on the downslope side of the flow and cannot explain the energetic oscillations recorded at the upper part of the slope. In addition, the development of eddies from baroclinic eddies are relatively slow. Plume water spilling over the sill and advancing with 20 cm s^{-1} can be expected to reach the mooring array F1–4 within 2–3 d, while baroclinic eddies formed in Tanaka's (2006) simulations reached a mature stage only after 17 d in their 'steep slope-high latitude' (SH) scenario, which has a slope, Coriolis parameter, flux and density difference appropriate for the Filchner overflow, albeit a different outflow geometry. Baroclinic instabilities are initialized on an initially steady current, and there are no observations or indications of such a flow downstream of the Filchner sill. In summary, the observations cannot be explained by baroclinic instabilities.

Eddies can also be generated in dense plumes through ‘vortex stretching’. This happens when the fluid above the dense layer is captured and stretched as the dense fluid descends the slope. To maintain its potential vorticity the upper layer begins to rotate, transmitting the motion barotropically to the lower layer (Lane-Serff and Baines, 1998). The eddies so formed are cyclonic, and capture a ‘dome’ of dense water below them. The observation of co-occurrent cyclonic motion (negative vorticity) and low temperatures for O35 and O6 agrees with this picture (O3 is observed mainly in the across-slope record at F3, and the method used to approximate vorticity therefore fails here). Theory suggests that eddies formed through vortex stretching are baroclinic, with a strong barotropic component (Lane-Serff and Baines, 1998). Scaling arguments imply that the baroclinic component is relatively large, although laboratory experiments showing a strong cyclonic motion in the lower layer (Lane-Serff and Baines, 2000) do cast some doubt on the theoretical scaling and on how strong the baroclinic component can be expected to be. The oscillations described here are all barotropic or close to barotropic. The frequency at which eddies form by vortex stretching is limited by the speed at which the domes ‘fill up’ and move away from the source. Based on laboratory experiments Lane-Serff and Baines (1998) found an empirical lower limit or a minimum period for eddy generation, which in the Filchner region would correspond to about 63 h or 2.6 d. The shortest oscillation (O35) is much shorter than 63 h and is not likely to be caused by vortex stretching (Lane-Serff, personal communication, 2008). Using parameters representative of the Filchner outflow Lane-Serff and Baines (2000) estimated that vortex stretching would cause eddy generation with a period of 3 d in the Filchner overflow, and their result is supported by idealized numerical simulations from the area (Wang et al., 2008), showing eddies, generated through vortex stretching, and a transport variability with a period of 3 d. The theoretical period is identical to the observed O3, suggesting that O3 is related to vortex stretching. Note, however, that even if the frequency of eddy generation may change, for example, as stratification or flux vary, vortex stretching can only be expected to generate one ‘period’ at a time. The data show a superposition of oscillations and O3 and O35 regularly observed simultaneously (see e.g. Figs. 9b–c and Fig. 10 in the Appendix). If vortex stretching and eddies are causing O3, the mechanism responsible for O35 and O6 remains to be found. Interestingly, the eddies generated in the model by Wang et al. (2008) seemed to form three ‘trains’ of eddies, localized at different levels on the slope and of which the lowest is associated with the subplumes observed at the deep side of the plume. Eddies on the upper part of the slope were smaller than those on the lower part of the slope (Wang, personal communication, 2008).

Dense domes of water trapped beneath an eddy will move along the sloping bottom with the Nof speed (Nof, 1983)

$$U_{\mathrm{Nof}} = \frac{g's}{f}, \tag{1}$$

where f is the Coriolis parameter, s the slope and $g' = g\frac{\Delta\rho}{\rho_0}$ the reduced gravity. If the oscillations are due to passing eddies, the Nof speed and the oscillation period give a scale for the eddy size ($L = U_{\mathrm{Nof}} T_{\mathrm{Oscillation}}/2$). A slope of $s = 0.01$– 0.03 (where the larger slope value refers to the shallow part of the slope) and $\Delta\rho = 0.1$ kg m^{-3} give Nof velocities of about 10–30 cm s^{-1} and consequently length scales of 5–20, 15–40 and 25–80 km for the O35, O3 and O6 oscillation, respectively. An estimate of possible eddy size can also be achieved from the simultaneous observations of the oscillations at the different moorings (F1–4), see Figs. 8a–c. The distance between the moorings F2 and F3 is 17.5 km, indicating that the O3 eddies would have a diameter around 20–40 km. If they were significantly smaller, they would not be recorded simultaneously at the two moorings, and if they were much larger, the oscillation would have been recorded also at F1 or F4. A similar argument can be applied to O6 (F3–4) and O35 (F1–3). These values agree relatively well with the ones deduced from the Nof speed, if one take into account that O35 (O6) is centred on the shallow, steep (deeper, less steep) part of the slope, where the higher (lower) Nof speed and the larger (smaller) size estimate is representative. In the simulations by Wang et al. (2008), the modelled eddies measured 20–40 km in diameter, and they were elongated in the along-slope direction. The estimated length scales can be compared with the internal Rossby radius, which is on the order of 5–10 km.

4.2.2. Continental shelf waves. Another possible explanation for the observed oscillations is coastally trapped waves or so-called CSW. These waves, as their name implies, are trapped along the shelf and propagate (in the Southern Hemisphere) with the coast to the left (i.e. westward around Antarctica) as a sequence of horizontal eddies with alternating sign (LeBlond and Mysak, 1978). Much like topographic Rossby waves, they owe their existence to the combined effect of rotation and variable water depth and they typically have amplitudes of a few centimetres, periods of several days and wavelengths much longer than the Rossby radius (Mysak, 1980). The CSW can be both barotropic and baroclinic and their amplitude decreases exponentially away from the shelf break. The waves are usually generated by atmospheric forcing or wind (Mysak, 1980), but other generation mechanisms are possible, such as interactions between currents and topography and variable discharge from the coast. The observed intensification of the diurnal tidal currents near the shelf break in the Weddell Sea is thought to be due to the excitation of shelf waves with tidal frequencies (Middleton et al., 1987; Robertson, 2005). In a laboratory setting, Whitehead and Chapman (1986) observed shelf waves to be generated by a low-density surface current flowing over a sloping bottom. Shelf waves could thus propagate into the area, or be generated locally, possibly by mechanisms related to the outflow itself.

Middleton et al. (1982) adapted a barotropic shelf wave model (Saint-Guily, 1976) for the Southern Hemisphere and the continental slope in the Filchner area. Based on data from the moorings west of Ridge 2, they provided evidence for the existence of shelf waves with periods of 3–60 d in the area (As mentioned before, the energy levels at these moorings are much lower than those observed east of Ridge 1, and neither O35, O3 nor O6 show a peak in the Fourier spectra from the shallow moorings). The authors suggest atmospheric forcing as a likely generation mechanism. Looking closer at O35 with respect to shelf waves and the Saint-Guily model, it is seen that the frequency would correspond to a wavelength of about 200 km and that the first mode is the only possible mode (see Middleton et al., 1982, fig. 10a). The first mode corresponds to CCW motion on the upper slope and a CW motion lower down with the transition occurring at roughly 1000-m depth. Mooring F1, located at 687-m depth, shows a strong CCW signal at O35, while F2, at 1180-m depth, shows a strong CW signal (weak CW signal at F3 and F4)—in agreement with the model (This pattern is not, as will be discussed later, unique for shelf waves). The observed oscillations are barotropic or close to barotropic, and strongest at the shallowest part of the slope. When concentrating on the F-moorings, it seems plausible that O35 may be related to propagating shelf waves, but D2 (1775 m) shows a relatively strong along-shelf oscillation at O35 and the older moorings, located west of Ridge 2 and close to the shelf break, show no O35 at all. The latter point could possibly be explained by interannual variability, that is, that the waves were not generated when the moorings west of the ridge were operating, or by the presence of the two ridges between the observation points, as relatively small topographic irregularities have been shown to scatter, reflect or degenerate barotropic shelf waves (Mysak, 1980). Shelf waves are strongest at the shelf break and could not satisfactorily explain the oscillations that are observed to be most energetic lower down on the slope, that is, O3 and O6. Shelf waves can travel far. The frequency (O35) is not mentioned by Fahrbach et al. (1992), who report on variability from current meter moorings placed on the continental slope further east on Kapp Norvegia (17°W), and it is not seen in data from current meter moorings on the continental slope on the eastern tip (45°W–55°W, 64°S) of the Antarctic Peninsula (von Gyldenfeldt et al., 2002) (O3 and O6 are not reported on Kapp Norvegia/the Antarctic Peninsula either). If the oscillations are due to shelf waves, the generation mechanism, and the preference for the observed period(s), remains to be explained.

The wavelet analysis suggests a possible relation between the oscillations and tidal motion, since, for example, O35 at D2 (Fig. 9) and O35 and O3 at F3 show modulations in amplitude with a period that would roughly correspond to the spring-neap tidal cycle, although the signal is neither clear nor consistent. Tidal motion can be expected not only to influence the transport of water from the Filchner Depression (a 14-d oscillation is apparent in a few of the records here), and thus the potential generation of eddies, but also to modify plume mixing and ambient stratification, and thus the transmission properties of CSW, in the region. As mentioned earlier, the tidal motion is enhanced along the shelf break as diurnal CSW are excited. Similar tidal shelf waves are observed elsewhere, for example, along the shelf break outside Spitsbergen (80°N). Interestingly, Nilsen et al. (2006) observe oscillations with a period of 35 h (i.e. identical to O35) in this region, which they, based on the dispersion equation given by an idealized numerical model, claim to be CSW of a higher mode and directly linked to the tidal CSW. The results cannot be directly transferred to the Filchner region, since they depend strongly on topography and background current, but they still suggest that there may be a link between the tidal CSW and the observed oscillations. Unfortunately, the properties of the coastal current following the shelf break are poorly known, making it difficult to apply a model such as the one used in Nilsen et al. (2006) to the region.

The rotation at the moorings for O35 (CCW at the top of the slope and CW further down), was shown to agree with the shelf wave model of Middleton et al. (1982). The observed pattern could, however, be given by any eddy-train, cyclonic, anticyclonic or alternating, travelling westwards along the slope and passing the mooring array with the eddy centre between F1 and F2. A mooring located on the shallower (deeper) side of an eddy travelling westwards will register a CCW (CW) motion, regardless of whether the eddy itself is cyclonic or anticyclonic, that is, rotating CCW or CW, see Fig. 8d. A mooring located near the centre of the eddy will register an oscillation in the across-slope component only. This pattern is readily recognized in Table 2 and in Figs. 8a–c, where CCW motion is found on the shallower moorings and CW motion on the deeper.

5. Conclusion

The flow of cold ISW emerging from the FRIS cavity through the Filchner Depression in the Weddell Sea has been described, based on a synthesis of CTD and current meter data. East of the two prominent ridges cross-cutting the slope close to 36°W, the plume generally appears as a well-defined, 100-300-m thick bottom layer with minimum temperatures close to the surface freezing point. West of the ridges the dense layer is warmer, more stratified and markedly thicker, with a thickness of up to 800 m. It is evident that intense mixing and entrainment must take place between the two plume ‘regimes’, probably in the ridge region. The ridges act to steer a potentially large part of the dense plume downslope, possibly dividing the plume in three as suggested by Foldvik et al. (2004).

In addition to tidal motion, three dominating oscillations, with periods of 35 h, 3 and 6 d, are present on the slope. The oscillations are episodic, seemingly barotropic, have a length scale (across the slope) of 20–40 km and appear to be separated geographically; the longer, 6-d oscillation occurs predominantly on the lower part of the slope, the shorter 35-h oscillation is stronger on the upper part of the slope and the 3-d oscillation in between. There are, however, exceptions. The variability is lower west of the two ridges and in the Filchner Depression, where only the 6-d oscillation is discernible. Three possible mechanisms generating oscillations in a plume or on a slope were suggested and discussed in relation to the observations: eddies generated by baroclinic instabilities; eddies generated by vortex stretching and CSW. It seems unlikely that the oscillations are due to baroclinic instabilities, but it is not possible, based on the available data and the current analysis, to determine whether one of the other candidates, a combination of them or even a fourth, possibly hitherto unexplained, mechanism is causing the observed oscillations. Further observational, theoretical and numerical studies are needed to explain the oscillations; the generation mechanisms, the preference for the observed frequencies and their interrelation, and finally their interaction with the ISW plume, the coastal current and the two ridges.

6. Acknowledgments

We thank all scientists and crew members who have been involved in the collection and preparation of the data. A special thank to the British Antarctic Survey (BAS), the Alfred Wegener Institute for Polar and Marine Research (AWI), L. Padman and A. Orsi for contributing with data. This is publication A202 in the Bjerknes publication series, and was accomplished as a part of the IPY Bipolar Atlantic Thermohaline Circulation (BIAC) project funded by the Research Council of Norway (Nr:176082). Suggestions and comments from G. Lane-Serff and three anonymous reviewers were greatly appreciated.

7. Appendix A: Complementary material

Oscillations similar to the ones describes in Section 3.2.1 but with longer periods (3 and 6 d) are observed on the slope and will be described in further detail below.

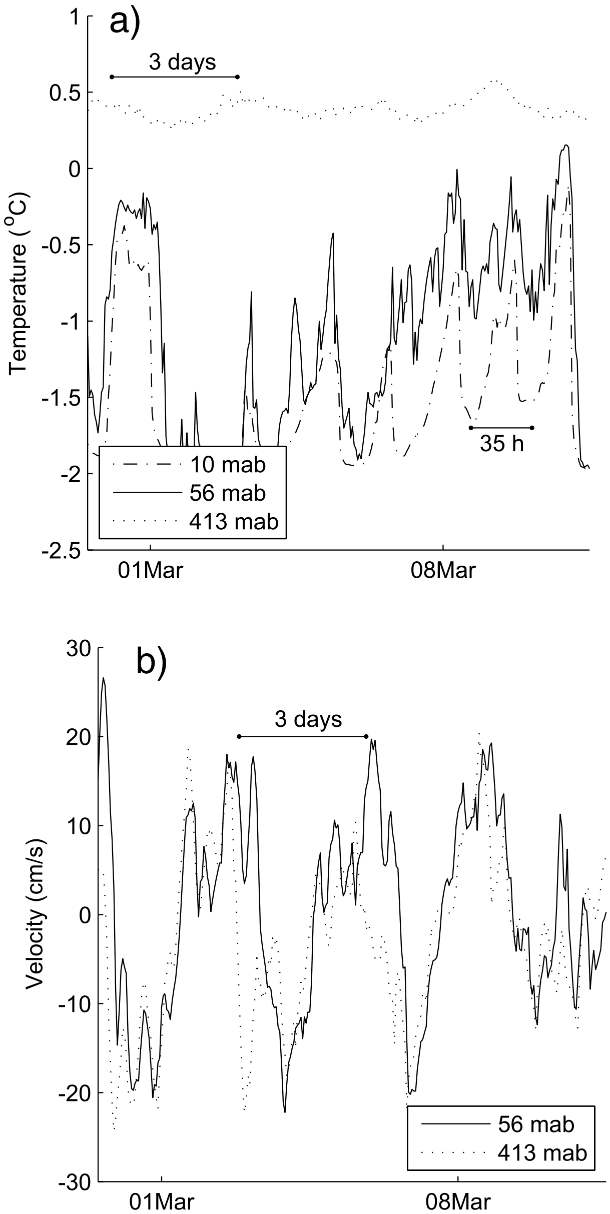

Fig. 10. (a) Temperature and (b) across-slope velocity (v) records from F3 (1637 m) in March 1998 showing a 3-d oscillation.

A1. 3-d oscillation

Figure 10 shows the temperature and velocity records from March 1998 from mooring F3, situated at 1637-m depth and probably on the lower side of the plume (see Fig. 1 for location). A three-days oscillation (O3) is apparent in the shallowest temperature record (433 mab), which is seen to oscillate between 0.3 and 0.4 °C. O3 is less clearly seen in the temperature records from the deeper instruments, which are, during the end of the period shown, dominated by a faster 35-h oscillation (O35).

O3 is clearly present in the across-slope velocity record (v), while the along-slope record (u, not shown) is, like the deeper temperature records, dominated by O35. The oscillation in v has an amplitude of 20 cm s^{-1}, and no clear vertical attenuation or phase shift during the period shown in Fig. 10. When considering the whole F3 record, however, a positive vertical phase shift for O3 (see Table 1) is apparent. At F2, located 17.5 km up the slope at 1180-m depth, O3 is present in both u and v, with no vertical phase shift. The oscillation at F2 is CCW.

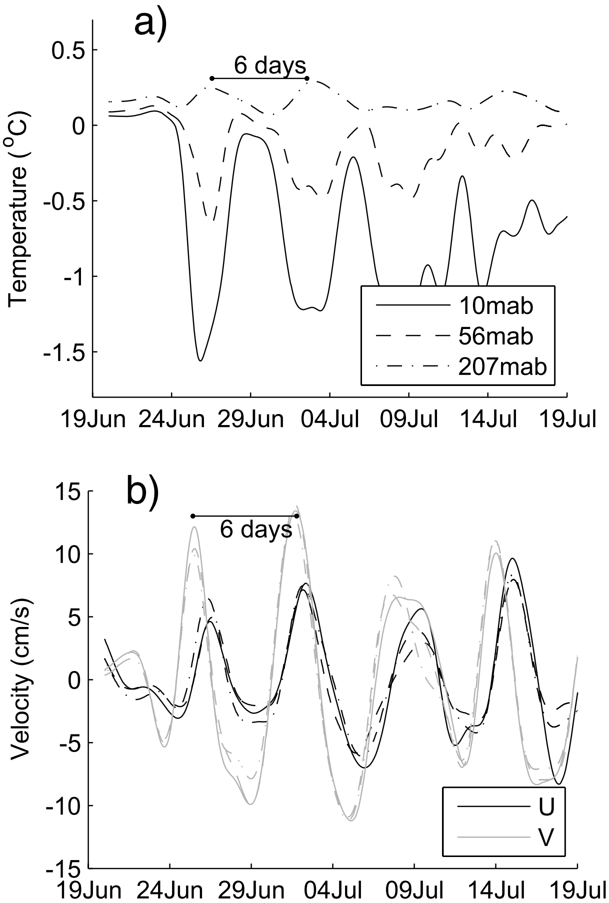

Fig. 11. (a) Temperature and (b) velocity in June 1998 showing a 6-d oscillation. The velocity records have been filtered (bandpassed, 3–15 d). The key in (a) is valid for both graphs.

A2. The 6-d oscillation

Mooring F4 is situated at 1984-m depth and is generally below the main path of the plume (see Fig. 3). Figure 11 shows velocity and temperature records from F4 during the winter months. A 6-d oscillation is seen at all depths, both in the temperature and velocity records, and its initiation is associated with a sudden drop in temperature at the lower instruments. The temperature decreases from 0 °C to below -1.7 °C in 12 h (unfiltered data, not shown), indicating that the WDW, which is usually surrounding the mooring, is replaced by cold plume water. The temperature continues to oscillate with a period of approximately 6 d for about a month, but the amplitude decreases and the temperature at the bottom-most instrument stabilizes. The shallowest instrument (207 mab) is never submerged in cold plume water and so the plume is always thinner than 200 m, in agreement with the mean thickness from the CTD data in Fig. 3b. The oscillation at the upper instrument is out of phase with the deeper ones: low temperatures at the bottom are coupled to a slight increase ($\sim$0.1 °C) in temperature at 207 mab.

There is a vertical shear in the mean current, with velocities increasing towards the bottom, but the oscillation in velocity is seemingly vertically homogeneous with an amplitude of 5–10 cm s^{-1} and no vertical phase shift (see Table 1). The velocity vectors trace out a CW ellipse in which the cold water is flowing with an eastward component, that is, opposite to the mean plume flow.

The oscillation is recorded simultaneously at F3, mainly in the along-slope record (u). As described in Section 3.2.1, the difference in velocity between the moorings is an indication of the vorticity, and, as in the 35h case, negative (positive) vorticity is associated with low (high) bottom temperatures.

Oscillations with the same 6-d period were recorded more than a decade earlier at mooring D1 (not shown). Mooring D1 was placed 100 m deeper than F4 and 9 km to the north in the vicinity of Ridge 1. At D1 the O6 oscillation is seen mainly in u (which is here the direction of the mean flow), parallel to, and seemingly restricted by Ridge 1. The amplitude at D1 is 35 cm s^{-1} and thus roughly equals to the mean speed (37 cm s^{-1}). The temperature record oscillates in phase with the velocities, with low temperatures (~ -1.8 °C) corresponding to high speeds ($\sim$70 cm s^{-1}), and high temperatures ($\sim$0 °C) to slow (or no) currents ($\sim$0 cm s^{-1}) (see Foldvik et al., 2004, fig. 12d). The flow at D1 can be characterized as pulses of cold high-speed plume water and intermittent quiescent periods when the mooring is submerged in WDW. The oscillation is seen at both 25 and 100 mab.

References

Broecker, W. S., Peacock, S. L., Walker, S., Weiss, R., Fahrbach, E. and co-authors. 1998. How much deep water is formed in the Southern Ocean?. *J. Geophys. Rese.-Oceans* **103**, 15 833–15 843.

Bruce, J. G. 1995. Eddies southwest of the Denmark Strait. *Deep-Sea Res. Part I* **42**, 13–29.

Cenedese, C. and Adduce, C. 2008. Mixing in a density driven current down a slope in a rotating fluid. *J. Fluid Mech.* **604**, 369–388.

Cenedese, C., Whitehead, J. A., Ascarelli, T. A. and Ohiwa, M. 2004. A dense current flowing down a sloping bottom in a rotating fluid. *J. Phys. Oceanogr.* **34**, 188–203.

Darelius, E. 2008. Topographic steering of dense overflow plumes: laboratory experiments with V-shaped canyons and ridges. *Deep-Sea Rese. Part I*, **55**, 1021–1034.

Darelius, E. and Wåhlin, A. 2007. Downward flow of dense water leaning on a submarine ridge. *Deep-Sea Res. Part I* **54**, 1173–1188.

Deacon, G. 1937. The hydrology of the Southern Ocean. *Discov. Report* **15**, 1–24.

Emery, W. J. and Thomson, R. E. 2001. *Data Analysis Methods in Physical Oceanography 2nd and revised Edition*. Elsevier, Amsterdam

Etling, D., Gelhardt, F., Schrader, U., Brennecke, F., Kuhn, G. and co-authors. 2000. Experiments with density currents on a sloping bottom in a rotating fluid. *Dyn. Atmos. Oceans* **31**, 139–164. Sp. Iss SI.

Ezer, T. 2006. Topographic influence on overflow dynamics: Idealized numerical simulations and the Faroe Bank Channel overflow. *J. Geophys. Res.* **111**, doi:10.1029/2005JC003195.

Fahrbach, E., Rohardt, G. and Krause, G. 1992. The Antarctic coastal current in the Southeastern Weddell Sea. *Polar Biol.* **12**, 171–182.

Fahrbach, E., Harms, S., Rohardt, G., Schroder, M. and Woodgate, R. A. 2001. Flow of bottom water in the northwestern Weddell Sea. *J. Geophys. Res.-Oceans* **106**, 2761–2778.

Foldvik, A. and Gammelsrød, T. 1988. Notes on southern-ocean hydrography, sea-ice and bottom water formation. *Palaeogeogr. Palaeoclimatol. Palaeo-ecol.* **67** 3–17.

Foldvik, A., Gammelsrød, T. and Tørresen, T. 1985a. Hydrographic observations from the Weddell Sea during the Norwegian antarctic Research Expedition 1976/1977. *Polar Res.* **3**, 177–193.

Foldvik, A., Gammelsrød, T. and Tørresen, T. 1985b. Physical oceanography studies in the Weddell Sea during the Norwegian antarctic Research Expedition 1978/79. *Polar Res.* **3**, 195–207.

Foldvik, A., Middleton, J. H. and Foster, T. D. 1990. The tides of the southern Weddell Sea. *Deep-Sea Rese. Part A-Oceanogr. Res. Papers* **37**, 1345–1362.

Foldvik, A., Gammelsrød, T., Østerhus, S., Fahrbach, E., Rohardt, G. and co-authors. 2004. Ice shelf water overflow and bottom water formation in the southern Weddell Sea. *J. Geophys. Res.-Oceans* **109**, doi:10.1029/2003JC002008.

Foster, T. D. and Carmack, E. C. 1976. Frontal zone mixing and Antarctic Bottom Water formation in the Southern Weddell Sea. *Deep-Sea Res.* **23**, 301–317.

Geyer, F., Østerhus, S., Hansen, B. and Quadfasel, D. 2006. Observations of highly regular oscillations in the overflow plume downstream of the Faroe Bank Channel. *J. Geophys. Res.* **111**, doi:10.1029/2006JC003693.

Girton, J. B. and Sanford, T. B. 2003. Descent and modification of the overflow plume in the Denmark Strait. *J. Phys. Oceanogr.* **33**, 1351–1364.

von Gyldenfeldt, A. B., Fahrbach, E., Garcia, M. A. and Schrøder, M. 2002. Flow variability at the tip of the Antarctic Peninsula. *Deep-Sea Res. Part II* **49**, 4743–4766.

Høyer, J. L. and Quadfasel, D. 2001. Detection of deep overflows with satellite altimetry. *Geophys. Res. Lett.* **28**, 1611–1614.

Jiang, L. and Garwood, R. W. 1996. Three-dimensional simulations of overflows on continental slopes. *J. Physi. Oceanogr.* **26**, 1214–1233.

Killworth, P. 1977. Mixing on the Weddell Sea continental slope. *Deep-Sea Res.* **24**, 427–448.

Killworth, P. 2001. On the rate of descent of overflows. *J. Geophysi. Res.-Oceans* **106**, 22 267–22 275.

Käse, R. H., Girton, J. B. and Sanford, T. B. 2003. Structure and variability of the Denmark Strait Overflow: model and observations. *J. Geophys. Res.-Oceans* **108**, doi:10.1029/2002JC001548.

Lane-Serff, G. 2001. Overflows and cascades. In: *Encyclopedia of Ocean Sciences*, (eds J. Steele, S. Thorpe and K. Turekian). Elsevier, Amsterdam.

Lane-Serff, G. F. and Baines, P. G. 1998. Eddy formation by dense flows on slopes in a rotating fluid. *J. Fluid Mech.* **363**, 229–252.

Lane-Serff, G. and Baines, P. G. 2000. Eddy formation by overflows in stratified water. *J. Phys. Oceanogr.* **30**, 327–337.

LeBlond, P. and Mysak, L. 1978. Waves in the ocean. In: *Elsevier Oceanography Series* Volume 20. Elsevier Scientific Publishing Company,Amsterdam, the Netherlands.

Matsumura, Y. and Hasumi, H. 2008. A non-hydrostatic ocean model with a scalable multigrid Poisson solver. *Ocean Model.* **24**, 15–28.

Middleton, J. H., Foster, T. D. and Foldvik, A. 1982. Low-frequency currents and continental-shelf waves in the southern Weddell Sea. *J. Phys. Oceanogr.* **12**, 618–634.

Middleton, J. H., Foster, T. D. and Foldvik, A. 1987. Diurnal shelf waves in the southern Weddell Sea. *J. Phys. Oceanogr.* **17**, 784–791.

Miller, H. and Oerter, H. 1990. Die Expedition ANTARKTIS-V mit FS Polarstern 1986/87, Bericht von den Fahrtabschnitten ANT-V/4-5. *Reports on Polar Research. Technical Report 57*, Alfred Wegener Institute for Polar and Marine Research, Bremerhaven, Germany.

Mysak, L. 1980. Recent advances in shelf wave dynamics. *Rev. Geophys. Space Phys.* **18**, 211–241.

Nicholls, K., Padman, L., Schrøder, M., Woodgate, R., Jenkins, A. and co-aothors. 2003. Watermass modification over the continental shelf north of Ronne Ice Shelf, Antarctica. *J. Geophys. Res.* **108**, doi:10.1029/2002JC001713.

Nilsen, F., Gjevik, B. and Schauer, U. 2006. Cooling of the West Spitsbergen Current: Isopycnal diffusion by topographic vorticity waves. *J. Geophys. Res.* **111**, C08012, doi:10.1029/2005JC002991.

Nof, D. 1983. The translation of isolated cold eddies on a sloping bottom. *Deep-Sea Res. Part A* **30**, 171–182.

Orsi, A. and Whitworth, I. 2004. *Hydrographic Atlas of the World Ocean Circulation Experiment (WOCE). Volume 1: Southern Ocean*, Internationsal WOCE Project Office, Southampthon, UK (http://woceatlas.tamu.edu)

Orsi, A. H, Johnson, G. C. and Bullister, J. L. 1999. Circulation, mixing, and production of Antarctic Bottom Water. *Prog. Oceanogr.* **43**, 55–109.

Robertson, R. 2005. Baroclinic and barotropic tides in the Weddell Sea. *Antarct. Sci.* **17**, 461–474.

Saint-Guily, B. 1976. Sur la propagation des ondes de seconde classe le long d'un talus continental. *C.R. Acad. Sci. Paris* **B282**, 141–144.

Schlitzer, R. 2007. Assimilation of radiocarbon and chlorofluorocarbon data to constrain deep and bottom water transports in the world ocean. *J. Phys. Oceanogr.* **37**, 259–276.

Smith, P. C. 1976. Baroclinic instability in Denmark Strait Overflow. *J. Phys. Oceanogr.* **6**, 355–371.

Smith, P. C. 1977. Experiments with viscous source flows in rotating systems. *Dyn. Atmos. Oceans* **1**, 241–272.

Spall, M. A. and Price, J. F. 1998. Mesoscale variability in Denmark Strait: the PV outflow hypothesis. *J. Phys. Oceanogr.* **28**, 1598–1623.

Swaters, G. E. 1991. On the baroclinic instability of cold-core coupled density fronts on a sloping continental-shelf. *J. Fluid Mech.* **224**, 361–382.

Tanaka, K. and Akitomo, K. 2001. Baroclinic instability of density current along a sloping bottom and the associated transport process. *J. Geophys. Rese.-Oceans* **106**, 2621–2638.

Torrence, C. and Compo, G. 1997. A practical guide to wavelet analysis. *Bull. Am. Meteorol. Soc.* **79**, 61–78.

Wåhlin, A. K. 2002. Topographic steering of dense currents with application to submarine canyons. *Deep-Sea Res. Part I* **49**, 305–320.

Wåhlin, A. K. and Walin, G. 2001. Downward migration of dense bottom currents. *Environ. Fluid Mech.* **1**, 257–259.

Wåhlin, A. K., Darelius, E., Cenedese, C. and Lane-Serff, G. 2008. Laboratory observations of enhanced entrainment in the presence of submarine canyons and ridges. *Deep-Sea Res. Part I*, **55**, 737–750.

Wang, Q., Danilov, S. and Schröter, J. 2008. Bottom water formation in the southern Weddell Sea and the influence of submarine ridges: idealized numerical simulations. *Ocean Model.*, doi:10.1016/j.ocemod.2008.08.003.

Whitehead, J. A. and Chapman, D. C. 1986. Laboratory observations of a gravity current on a sloping bottom—the generation of shelf waves. *J. Fluid Mech.* **172**, 373–399.

Wilfried, J. and Oerter, H. 1997. Die Expedition ANTARKTIS-XII mit FS Polarstern 1995, Bericht vom Fahrtabschnitt ANT-XII/3. Reports on Polar Research. *Technical Report 219*,Bremerhaven, Germany.